



저작자표시-비영리-변경금지 2.0 대한민국

이용자는 아래의 조건을 따르는 경우에 한하여 자유롭게

- 이 저작물을 복제, 배포, 전송, 전시, 공연 및 방송할 수 있습니다.

다음과 같은 조건을 따라야 합니다:



저작자표시. 귀하는 원저작자를 표시하여야 합니다.



비영리. 귀하는 이 저작물을 영리 목적으로 이용할 수 없습니다.



변경금지. 귀하는 이 저작물을 개작, 변형 또는 가공할 수 없습니다.

- 귀하는, 이 저작물의 재이용이나 배포의 경우, 이 저작물에 적용된 이용허락조건을 명확하게 나타내어야 합니다.
- 저작권자로부터 별도의 허가를 받으면 이러한 조건들은 적용되지 않습니다.

저작권법에 따른 이용자의 권리는 위의 내용에 의하여 영향을 받지 않습니다.

이것은 [이용허락규약\(Legal Code\)](#)을 이해하기 쉽게 요약한 것입니다.

[Disclaimer](#)

이학박사 학위논문

Studies on Optical Field  
Confinement in Nanogaps and Its  
Applications as Photoresist  
Polymerization

나노갭 안에서 일어나는 전기장 구속과 이를  
이용한 포토레지스트 중합에 대한 연구

2019 년 8 월

서울대학교 대학원  
물리천문학부 물리학전공  
박 응 규

# Studies on Optical Field Confinement in Nanogaps and Its Applications as Photoresist Polymerization

지도 교수 홍 성 철

이 논문을 이학박사 학위논문으로 제출함  
2019 년 8 월

서울대학교 대학원  
물리천문학부 물리학전공  
박 용 규

박용규의 이학박사 학위논문을 인준함  
2019 년 8 월

위 원 장 \_\_\_\_\_ 노 태 원 \_\_\_\_\_ (인)

부위원장 \_\_\_\_\_ 홍 성 철 \_\_\_\_\_ (인)

위 원 \_\_\_\_\_ 박 철 환 \_\_\_\_\_ (인)

위 원 \_\_\_\_\_ 김 도 헌 \_\_\_\_\_ (인)

위 원 \_\_\_\_\_ 정 문 석 \_\_\_\_\_ (인)

# Abstract

In this work, photoresist polymerization near the nanogap with feature sizes much smaller than the diffraction limit was discussed. Firstly, how to make the deep-subwavelength gap was presented. I used two different types of waves (ultraviolet light and terahertz waves) for the photoresist polymerization experiments, therefore I used different gap fabrication methods for each experiment. Then photoresist polymerization using standard i-line ultraviolet light and nanogap has been demonstrated to enable nanolithographic experiments below the diffraction limit. In addition, the photoresist polymerization was realized by using the intense terahertz light, overcoming the lack of photon energy. These experiments have been verified by finite element method simulation or the theoretical calculations and confirmed that our nanostructures could realize the subwavelength scale photoresist polymerization. This study will present a great potential for various nano-photochemistry experiments and provide new insights.

**Keywords:** nanogap, polymerization, subwavelength

**Student Number:** 2013-20367

# Table of Contents

|  |    |
|--|----|
| Chapter 1. Introduction .....  | 1  |
| Chapter 2. Nanogap fabrication methods .....   | 4  |
| 2.1 Fabrication of sub-10 nm feature chromium nanogaps<br>.....                                    | 4  |
| 2.2 Fabrication of terahertz nano-slot antennas using a focused<br>ion beam .....                  | 13 |
| 2.3 Fabrication of terahertz-resonant bowtie nanoantennas<br>using electron-beam lithography ..... | 16 |
| Chapter 3. Subwavelength lithography using chromium<br>nanogaps .....                              | 19 |
| 3.1 Introduction.....  | 19 |
| 3.2 Near-field optical lithography .....   | 21 |
| 3.3 Finite element method simulation.....  | 24 |
| 3.4 Experimental details.....  | 26 |
| 3.5 Resist development & lift-off images .....   | 27 |
| 3.6 Conclusion.....  | 31 |
| Chapter 4. Terahertz-driven polymerization of resists in<br>nanoantennas .....                     | 32 |
| 4.1 Introduction.....  | 32 |
| 4.2 Terahertz wave & terahertz time-domain spectroscopy  |    |

|  |           |
|--|-----------|
| .....                                      | 34        |
| 4.3 Kirchhoff integral formalism.....      | 41        |
| 4.4 Experimental details and results ..... | 44        |
| 4.5 Finite element method simulation.....  | 52        |
| 4.6 Tunneling current measurement .....    | 54        |
| 4.7 Conclusion.....                        | 58        |
| <b>Chapter 5. Conclusion .....</b>         | <b>59</b> |
| <b>Bibliography .....</b>                  | <b>60</b> |
| <b>요약 (국문초록).....</b>                      | <b>69</b> |
| <b>List of publications.....</b>           | <b>70</b> |
| <b>Conferences .....</b>                   | <b>71</b> |

# List of Figures

**Figure 2.1** Schematic diagram of chromium nanogap fabrication processes. (a) Chromium/aluminum/chromium trilayer patterning by photolithography & lift-off. (b) First aluminum etching. (c) Aluminum oxide deposition by using the atomic layer deposition method. (d) Second chromium layer deposition. (e) Second aluminum etching. ....10

**Figure 2.2** Effect of the dented-overhang structures. (a) Chromium nanogap fabrication without dented-overhang structures can make unwanted debris in the vicinity of the nanogap. (b) Clean chromium nanogap samples can be fabricated by using the dented-overhang structures. ....11

**Figure 2.3** Scanning & transmission electron microscope images of the chromium nanogap. (a) Top-view image of chromium nanogap arrays. (b) Top-view image of the chromium nanogap extended over several tens of microns. (c) Magnified image of (b). (d) Cross-section image of the chromium nanogap taken by transmission electron microscopy.. ....12

**Figure 2.4** Scanning electron microscope image of the terahertz nano-slot antenna.....14

**Figure 2.5** Scanning electron microscope image of the square-

|   |    |
|---|----|
| shaped, terahertz nano-slot antenna.....  | 15 |
| <b>Figure 2.6</b> Scanning electron microscope image of the terahertz-resonant bowtie nanoantenna.....  | 18 |
| <b>Figure 3.1</b> Evanescent near-field optical lithography. ....   | 22 |
| <b>Figure 3.2</b> Various near-field optical lithography techniques. (a)Optical nanolithography experiment using superlens. (b) Optical nanolithography system with a contact probe.....  | 23 |
| <b>Figure 3.3</b> Calculated electric field distribution by using the finite element method simulation.....   | 25 |
| <b>Figure 3.4</b> Atomic force microscope image of the developed photoresist.....   | 29 |
| <b>Figure 3.5</b> (a) Dark-field optical microscope image of the chromium nanogap. (b) Optical microscope image of the patterned metal rings on a silicon substrate. (c) Scanning electron microscope image of the metal square ring. (d) Scanning electron microscope image of the metal wire..... | 30 |
| <b>Figure 4.1</b> The terahertz wave lies between the infrared light and the microwave.....   | 37 |
| <b>Figure 4.2</b> Concept of the confined terahertz electromagnetic waves in the metallic nanogap.....  | 38 |
| <b>Figure 4.3</b> Schematics of the oscillator-based, time-domain   |    |

|   |    |
|---|----|
| terahertz spectroscopy setup.....   | 39 |
| <b>Figure 4.4</b> Schematics of the high–power terahertz generation by optical rectification using the tilted–pulse–front.....  | 40 |
| <b>Figure 4.5</b> Schematics of a diffraction geometry of slit arrays in a metallic screen.....   | 43 |
| <b>Figure 4.6</b> Schematics of high–power terahertz wave illumination to the photoresist/metal nano–slot antenna sample.....   | 47 |
| <b>Figure 4.7</b> Terahertz wave–assisted photoresist polymerization in nano–slot antenna. (a) The photoresist is cross–linked at the center of the terahertz nano–slot antenna. (b) scanning electron microscope image of the nano–slot antenna before the photoresist coating. (c) scanning electron microscope image of the nano–slot antenna after the high power terahertz wave illumination and the photoresist polymerization..... | 48 |
| <b>Figure 4.8</b> Terahertz wave–assisted photoresist polymerization in bowtie nanoantenna. (a) scanning electron microscope image of the terahertz–resonant bowtie nanoantenna before photoresist coating. (b) scanning electron microscope image of the bowtie nanoantenna after the high power terahertz wave illumination and the photoresist polymerization.....   | 49 |
| <b>Figure 4.9</b> Measured field enhancement factor of the square–  |    |

|   |    |
|---|----|
| shaped nano-slot antenna depending on the frequencies.....  | 50 |
| <b>Figure 4.10</b> Terahertz wave-assisted photoresist polymerization in squared-shaped terahertz nano-slot antenna. (a) scanning electron microscope image of the square-shaped nano-slot antenna before the photoresist coating. (b) scanning electron microscope image of the square-shaped nano-slot antenna after the high power terahertz wave illumination and the photoresist polymerization..... | 51 |
| <b>Figure 4.11</b> Calculation of the electric field distribution in the terahertz-resonant bowtie nanoantenna by using the finite element method simulation.....   | 53 |
| <b>Figure 4.12</b> (a) Measured/calculated electric current depending on the incident terahertz field amplitude. (b) Fowler-Nordheim plot of the measured/calculated electric current.....  | 57 |

# Chapter 1. Introduction

Nano-optics is a study of the interaction between the light and nanostructures below the diffraction limit. One of the best-known phenomena in nano-optics is the extraordinary optical transmission[1], which is that the light transmission is greatly enhanced in the subwavelength aperture array arranged periodically. The extraordinary optical transmission has been observed and its physical interpretation has been suggested in the various optical region.

For example, in the near-infrared region, the extraordinary optical transmission could be explained by surface plasmon resonance and constructive interference of the light[1]. The extraordinary transmission through the terahertz nano-slit or nano-slot antenna could be explained by the capacitive coupling[2,3].

One of the characteristics of the extraordinary transmission through the terahertz nano-slit or nano-slot antenna is the increase of the normalized-to-area transmittance when the width of the gap is reduced[4]. That is, the terahertz field enhancement and field confinement can be increased if the gap width becomes narrower. Therefore, several attempts have been made to reduce the gap size

to increase terahertz field enhancement and field confinement. In 2013 and 2015, 1 nm or 0.3 nm wide gap was successfully fabricated by using atomic layer lithography, which was a combined method of photolithography, atomic layer deposition or chemical vapor deposition, and ultimate field enhancement and field confinement could be achieved in the terahertz range [5–7].

The nanogap made by the atomic layer lithography also has high field enhancement factors and field confinement in the various optical region [5,8–11]. Therefore, various research has been conducted in numerous fields such as terahertz nonlinear transmission [6,12,13], terahertz rectification [14], surface-enhanced Raman scattering [15], surface-enhanced infrared absorption [16].

The technology in nano-optics also has the potential to be widely used in photochemistry because it can enhance the optical electric field and confine the light. Nano-optics can be used to perform precise spatial control and increase the yield of chemical reactions. Various photochemical experiments including polymerization [17–29], water splitting [30–43],  $H_2$  dissociation [44–46] have been performed on various nanoantenna structures. In particular, various studies using photoresist polymerization have been carried out, because it was easy to visualize the optical field near the nanoantenna, and various applications such as nanolithography [17–19] and

selective functionalization [28] could be applied.

Since the nanogap has an extremely small gap size (i.e. huge field confinement) and high field enhancement factor, it can be used to increase local photochemical reaction. Therefore, it is worth investigating whether nanogaps can be used in photochemistry. In particular, using the above-mentioned properties of the photoresist polymerization, it is necessary to study whether the nanogap is suitable for photochemistry.

In this thesis, I provided details of two experiments about nanogap and photoresist polymerization. First, I proposed how to make nanogap in various ways. Then the details of nanolithography experiments using the ultraviolet light and chromium nanogap were discussed. After that, methods of photoresist polymerization using intense terahertz pulses and metallic nanogaps were discussed. All the experiments were justified by the finite element method simulation or theoretical calculations.

# Chapter 2. Nanogap fabrication methods

## 2.1 Fabrication of sub-10 nm feature chromium nanogaps

For polymerization experiments using ultraviolet lights, sub-10 nm feature chromium nanogap was made. Conventional nanogaps fabricated using the atomic layer lithography were made of gold or silver for optical[8,15,47], near-infrared[9,48], infrared[16], terahertz[5-7,11-14,49-61], or microwave[10] applications. However, in the ultraviolet regions, gold or silver had a low extinction coefficient and was unsuitable for nanolithography experiments. Chromium was much better at blocking the ultraviolet light. However, previous nanogap fabrication methods proposed in atomic layer lithography were not suitable for chromium nanogaps. Mechanical exfoliation method[5] was impossible since chromium has good adhesion to alumina. The nanogap fabrication method using ion milling[49] was possible to make chromium nanogaps, but this method required an additional ion milling machine, so the whole procedure is expensive and time-consuming. To overcome such experimental limits, I invented an easy and cost-effective method of making sub-10 nm feature chromium nanogap arrays on quartz substrates using photolithography, atomic layer deposition, and

chemical etching. During the fabrication process, I could bypass the unnecessary ion milling process by using a dented-overhang structure as a sacrificial layer.

The schematic diagram of a process for fabricating chromium nanogap was shown in Fig 2.1. Firstly, hexamethyldisilazane was spin-coated at 4000 rpm for 60 s onto the transparent quartz substrate. The thickness of the quartz substrate was 500  $\mu\text{m}$ . Then the sample was baked at 90  $^{\circ}\text{C}$  for 60 s. After baking the hexamethyldisilazane, the commercially available photoresist (AZ5214-E, AZ Electronic Materials) was spin-coated onto the hexamethyldisilazane. The spin coating rate was at 6000 rpm for 60 s, followed by soft-baking at 90  $^{\circ}\text{C}$ . The sample was exposed to ultraviolet light using an i-line mask aligner (Karl Süss MJB-3, Süss Microtec), with a photomask of desired micropatterns. In this photomask, the microstructures were square arrays with a side length of 50  $\mu\text{m}$  with 100  $\mu\text{m}$  periodicities. The exposure time was 7 s. After the first exposure to the ultraviolet light, the sample was hard-baked at 115  $^{\circ}\text{C}$  for 85 s. Then the second exposure to the ultraviolet light was carried out for the image reversal process. In this process, I didn't use photomask to expose the whole sample to the ultraviolet light, and the exposure time is 17 s. Finally, the exposed photoresist was developed by using commercially available

developer (AZ 500 MIF developer, AZ Electronic Materials) for 20 s, and the sample was cleaned by deionized water and dried in nitrogen gas. If necessary, we repeated the development and cleaning process with shorter times. After finishing the photolithography process, I deposited chromium/aluminum/chromium trilayers on the patterned photoresist layer by using electron beam evaporator (KVE-E2000, Korea Vacuum Tech). The thickness of each layer was 50 nm, 100 nm, and 20 nm, respectively. The deposition rate was 1 Å/s. I used acetone to remove the unwanted photoresist layers and to pattern the metal trilayers on the substrate. Then, I cleaned the sample by using deionized water and nitrogen gas (Figure 2.1 (a)). In the trilayers, the aluminum layer was used as a sacrificial layer. The sacrificial layer was etched for 10 s by 0.2 M sodium hydroxide solution. In this process, it should be noted that the aluminum layer was not completely etched out, but only dented. The top and bottom of the aluminum layer were blocked by the chromium layer, so only the sidewalls of the aluminum layer were etched, thus denting the structure (Figure 2.1 (b)). After the first etch process to create the dented overhang layers, a 5-nm-thick aluminum oxide thin film was deposited by using thermal atomic layer deposition at 200 °C (Lucida™ D series, NCD Tech.). In the atomic layer deposition process, I pulsed trimethylaluminum and water vapor

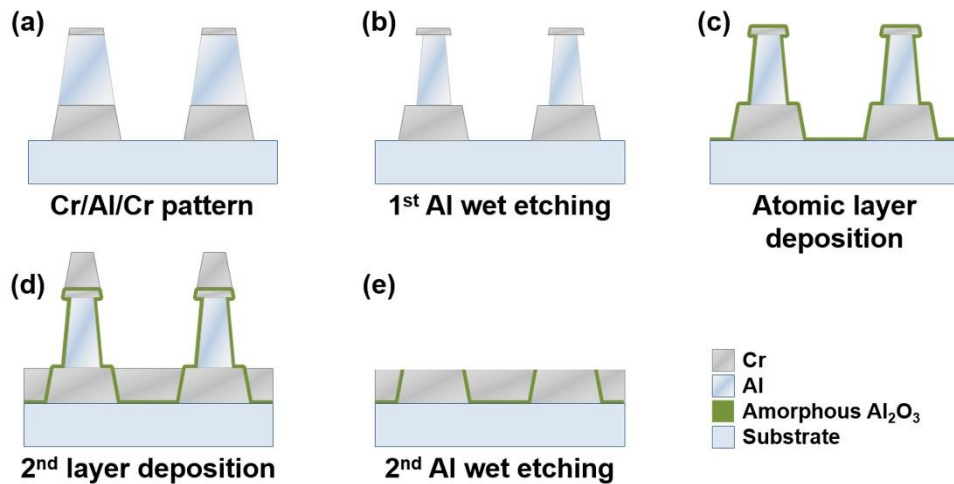
sequentially in 1.7 torrs for 0.1 s each. Then, nitrogen gas was used to purge the chamber for 10 s in 1.56 torr after each injection (Figure 2.1(c)). After the atomic layer deposition process, I deposited the second chromium layer inside the trench and above the trilayers. Since the entire sample was coated by a 5-nm-thick aluminum oxide layer, vertical dielectric nanogaps were created between the first chromium layer and the second chromium layer. In this deposition process, the deposition rate was 0.1 Å /s and the samples were rotated during the chromium evaporation. It was to prevent a shadowing effect (Figure 2.1 (d)). Finally, an unnecessary aluminum layer and a 20-nm-thick chromium layer on the aluminum layer were simultaneously removed by a wet etching process. Here I used a 0.5 M sodium hydroxide solution as an etchant. The samples were cleaned using deionized water and dried in nitrogen gas (Figure 2.1(e)).

Figure 2.2 compared the effect of a dented-overhang sacrificial layer and the normal aluminum layer. When the metals were deposited on the patterned photoresists, the sidewall of the metals produced by the lift-off process was not perpendicular to the quartz substrate. Therefore, if the aluminum layer was not etched slightly, the chromium could be piled up on the sidewalls of the aluminum layer as well as the quartz substrate when the second chromium deposition

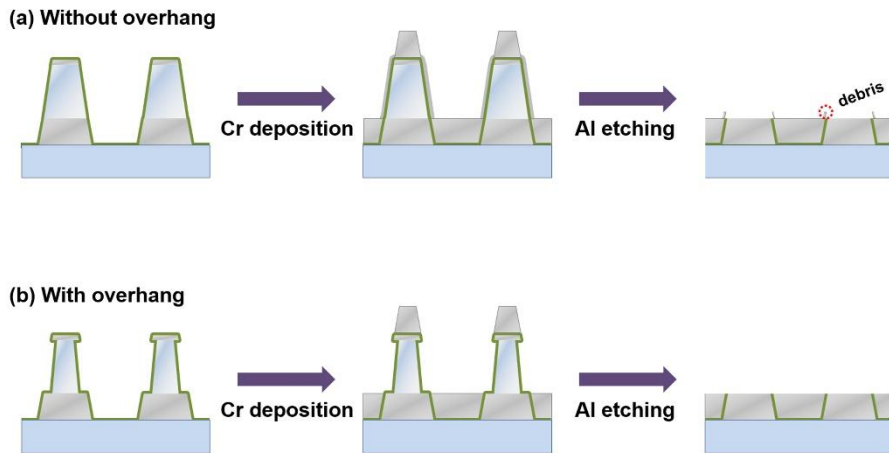
was performed. An undesirable chromium layer on the aluminum sidewalls prevents the aluminum sacrificial layer from being etched out. This made the aluminum remnants. Even though the aluminum sacrificial layer was completely removed, an undesirable chromium layer on the aluminum sidewall created debris in the vicinity of nanogap array. It should be noted that in nanolithography experiment, it was extremely important to remove the debris near the nanogap since the hard contact between the gap and photoresist determined the resolution of the contact lithography. If there is a space between the gap and photoresist, the evanescent wave from the gap will disappear. Therefore, we used the dented aluminum sacrificial layer to remove such debris. The dented-overhang structure was not blocked by chromium when the second deposition was performed. Because of the overhang structure, the chromium could not be piled up on the sidewall. As a result, the chromium as a second layer was deposited only inside the trench and above the trilayer. This made chromium nanogaps with a clean surface.

Figure 2.3 showed the scanning/transmission electron microscope images of the fabricated chromium nanogap samples. The chromium nanogap arrays fabricated on the transparent substrates were shown in Figure 2.3(a) and Figure 2.3(b). The fabricated nanogap had an extremely high aspect ratio since the photolithography was used to

make the microstructures. Figure 2.3(c) and 2.3(d) were the top-view and cross-section image of the nanogap. By using scanning and transmission electron microscopy, I could observe that the gap width was below 10 nm.



**Figure 2.1** A schematic diagram of a chromium nanogap fabrication processes. (a) Chromium/aluminum/chromium trilayer patterning by photolithography & lift-off. (b) First aluminum etching. (c) Aluminum oxide deposition by using the atomic layer deposition method. (d) Second chromium layer deposition. (e) Second aluminum etching.



**Figure 2.2** Effect of the dented-overhang structures. (a) Chromium nanogap fabrication without dented-overhang structures can make unnecessary debris in the vicinity of the nanogap. (b) Clean chromium nanogap samples can be fabricated by using the dented-overhang structures.

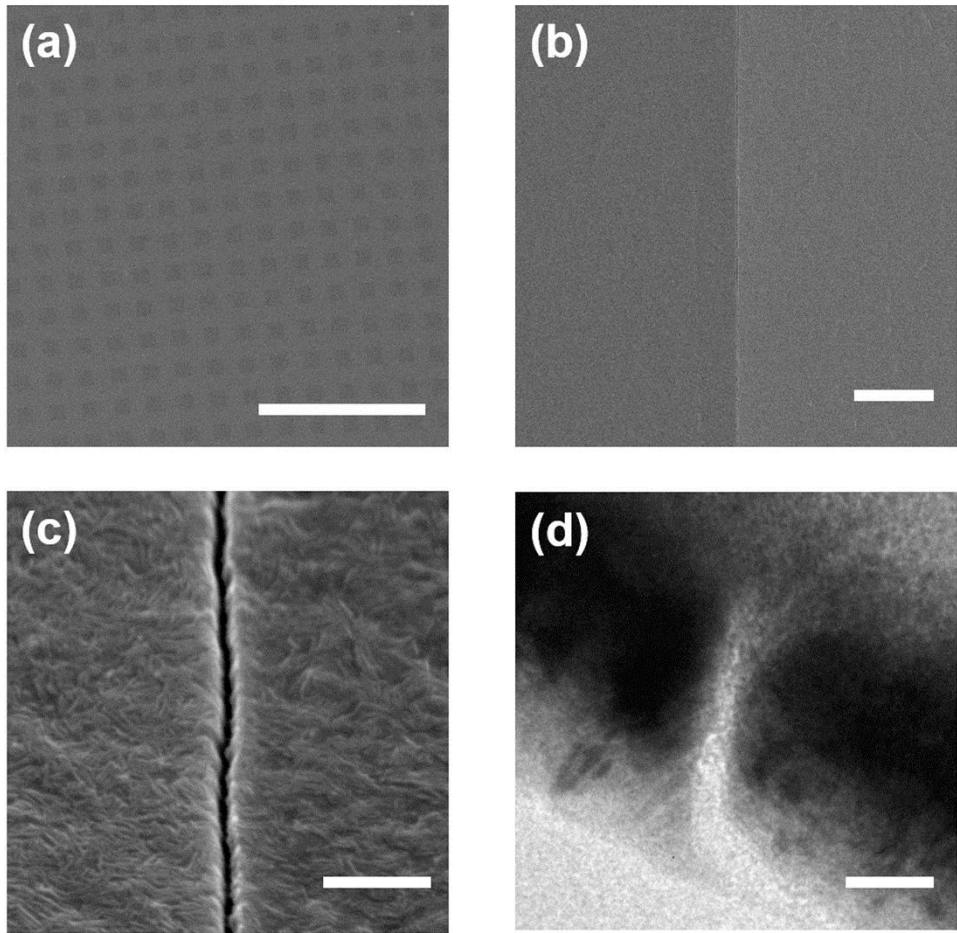


**Figure 2.3** Scanning & transmission electron microscope images of the chromium nanogap. (a) Top-view image of chromium nanogap arrays. (b) Top-view image of the one side of the chromium nanogap (c) Magnified image of (b). (d) Cross-section image of the chromium nanogap taken by transmission electron microscopy. Scale bars: (a) 500  $\mu\text{m}$ ; (b) 2  $\mu\text{m}$ ; (c) 200nm; (d) 20 nm.

## 2.2 Fabrication of terahertz nano-slot antennas using a focused ion beam

For terahertz-driven polymerization experiments, I made three different samples; terahertz-resonant nano-slot antenna arrays, square-shaped nano-slot antenna arrays, and terahertz-resonant bowtie nanoantenna arrays. To make two types of nano-slot antenna arrays, we firstly deposited 200-nm-thick silver films onto the substrates. For nano-slot antenna arrays, we patterned the slot antennas of length 60  $\mu\text{m}$ , period 120  $\mu\text{m}$ , and width 250 nm by focused ion beam technique. In this sample, the substrate was quartz. Figure 2.4 showed the scanning electron microscope image of the sample. A square-shaped slot antenna arrays were also fabricated by focused ion beam technique. The side length of the antenna was 60  $\mu\text{m}$ , and the width of the nanogap was 400 nm. In this case, the square-shaped nano-slot antenna was made on the glass substrate. Figure 2.5 showed the scanning electron microscope images of the sample.

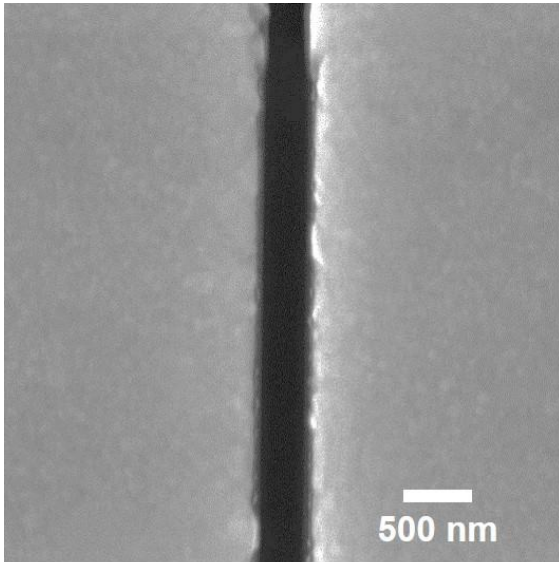


**Figure 2.4** Scanning electron microscope image of the terahertz nano-slot antenna.

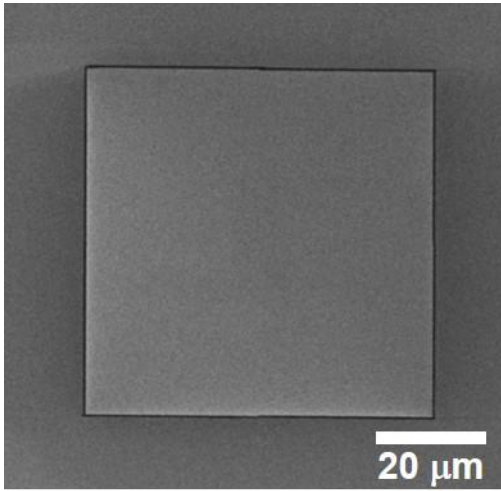


**Figure 2.5** Scanning electron microscope image of the square-shaped, terahertz nano-slot antenna.

## 2.3 Fabrication of terahertz-resonant bowtie nanoantennas using electron-beam lithography

To make bowtie-shaped, terahertz-resonant nanoantenna arrays, I used electron beam lithography and ion milling technique. Firstly, I deposited metal on the quartz substrate. Then a negative tone electron beam resists ma-N 2405 (Microchem) was spin-coated on the metal thin film (4000 rpm, 1 min). The thickness of the resist was about 500 nm, which was much thicker than the thickness of the metal thin film. The sample was then soft-baked at 150 °C for 90 s. I patterned bowtie antenna with 500 nm gap size by using field emission scanning electron microscopy (Mira 3 FE-SEM, Tescan). The period of the antennas was 360  $\mu\text{m}$ , the length of the long axis was 170  $\mu\text{m}$ , and the length of the short axis was 85  $\mu\text{m}$ , respectively. The unexposed electron beam resist was developed by a commercially available developer (ma-D 525, Microchem). Then the entire sample was physically etched by argon ion milling technique. In this process, I used argon ion miller (KVET-IM2000L, Korea Vacuum Tech) with 1.7 mA beam current and 80 V acceleration voltage. The patterned electron beam resists layer on the metal film blocked the metal layer from being etched out, which made bowtie-shaped metal nanoantennas. Finally, the unwanted electron beam

resists layer was removed by using acetone and isopropyl alcohol, cleaned by using deionized water, and dried in nitrogen gas. Figure 2.6 showed the scanning electron microscope image of the sample.

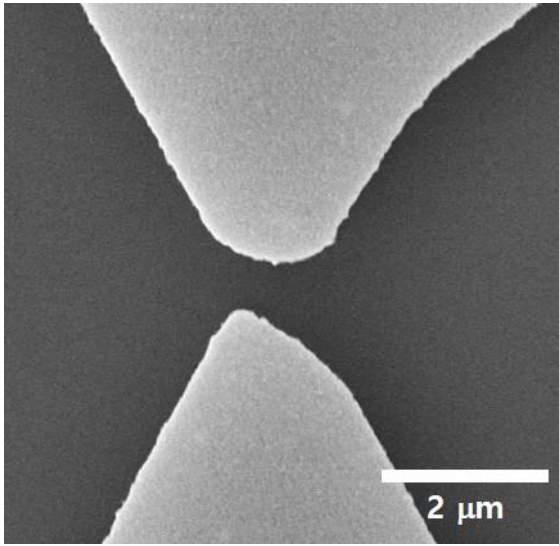


**Figure 2.6** Scanning electron microscope image of the terahertz-resonant bowtie nanoantenna.

# **Chapter 3. Subwavelength lithography**

## **using chromium nanogaps**

### **3.1 Introduction**

In recent years, various nanolithography techniques such as photolithography, electron beam lithography [62], nanoimprint lithography [63], and scanning probe lithography [64] have been developed for the ultimate limit of high density integrated circuits.

In particular, photolithography was the most widely used patterning technique in semiconductor industries because of its extremely high throughput and the ability to pattern structures with large uniformity. Several techniques have been proposed for patterning nanostructures using the ultraviolet light, such as extreme ultraviolet lithography [65–67], phase–shift mask [68], immersion lithography [69,70], multiple patterning lithography [71], evanescent near–field optical lithography [72,73], or plasmonic lithography [74–77]. As a result, the resolution of the photolithography has become tens of nanometers.

To make smaller patterns using photolithography, the feature size of the photomask should also become smaller. Also, for high

throughput, the uniformity of the pattern in the photomask should be maintained. However, photomasks were usually made by electron beam lithography. In the electron beam lithography, high-resolution patterning and large scale uniformity were conflicting with each other. Therefore, it was difficult to obtain nanometer-sized structures having large uniformity.

To overcome such an experimental limit, I invented the sub-10 nm feature chromium nanogap. The chromium nanogap was made by conventional photolithography, atomic layer deposition, and chemical etching. The feature size of the structure could be determined by the thickness of the aluminum oxide layer and the contour of the prepattern. Because photolithography is used in the prepattern, the structures can be uniformly formed with the 1 cm by 1 cm scale.

In this chapter, I showed the results of nanolithography by using the chromium photomask. At first, I briefly introduced the near-field optical lithography. Then I confirmed the results of the finite element method simulation to determine if the chromium nanogap was suitable for the evanescent near-field optical lithography. Then I performed the nanolithography experiments by using conventional mask aligner and chromium nanogap. Results of development images and lift-off images were also discussed in this section.

## 3.2 Near-field optical lithography

Near-field optical lithography is firstly suggested by M. M. Alkaisi *et al*[72]. In the experiment, they used evanescent optical near-field from the photomask to pattern the nanostructure below the diffraction limit. Figure 3.1 showed the concept of the evanescent near-field optical lithography [72]. Then various techniques including superlens [78] and contact probe [75] were used to obtain smaller patterns (Figure 3.2). These previous experiments used photomask made by using electron beam lithography or focused ion beam technique, which made it hard to obtain sub-10 nm feature nanostructures. Therefore, the resolution of the previous methods was fundamentally limited. In order to obtain the ultimate resolution of near-field lithography, it is necessary to make a photomask with smaller feature size. Therefore, I have created sub-10 nm feature chromium photomask to overcome the limitations of the conventional photomask and near-field lithography.

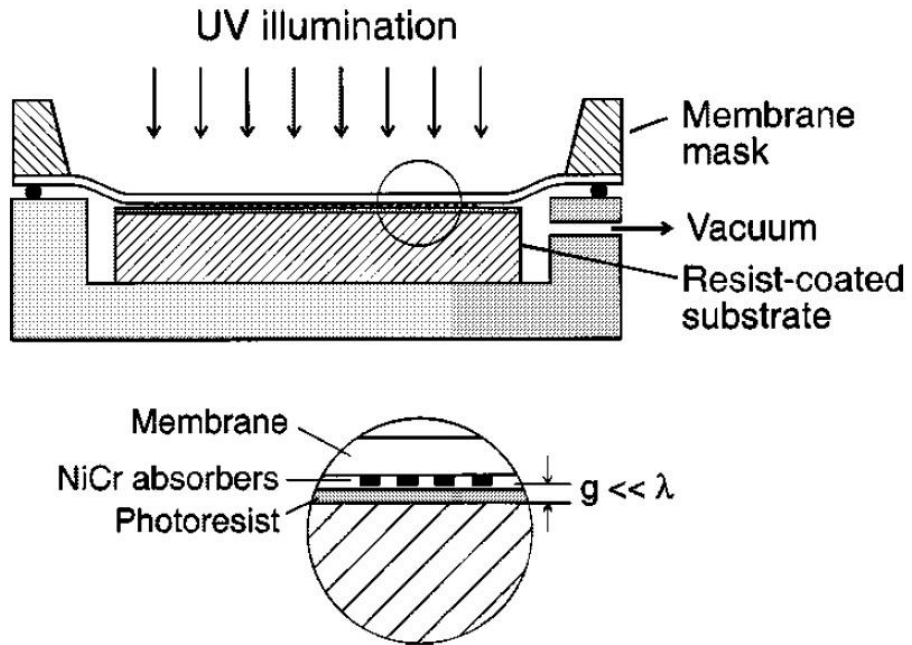
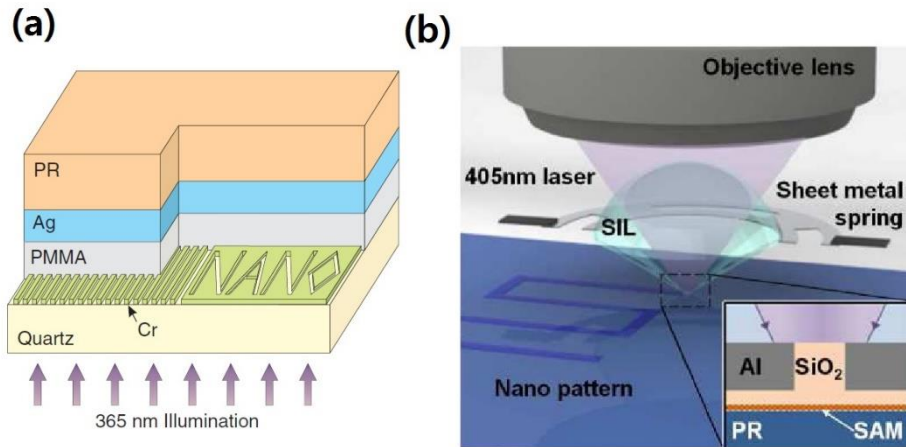


Figure 3.1 Evanescent near-field optical lithography.



**Figure 3.2** Various near-field optical lithography techniques.

(a) Optical nanolithography experiment using superlens. (b) Optical nanolithography system with a contact probe.

### 3.3 Finite element method simulation

Finite element method simulations were performed using COMSOL Multiphysics 5.3 software to verify that the chromium nanogap was suitable for nanolithography. In the simulation, the thickness of the metal was 50 nm and the gap width was 5 nm. The refractive index of the chromium at a wavelength of 365 nm was chosen from the data of Johnson and Christy [79]. The gap material was chosen as aluminum oxide, and the substrate was chosen as quartz. At the outside of the gap, the material was chosen as an air.

The electric field distribution was shown in Figure 3.3. It can be confirmed that the electric field was confined inside the gap. On the air-side of the gap, the magnitude of the electric field was about three times smaller than that of the incident field. In terms of the light intensity, it was about ten times smaller than that of the incident field. However, the dose in photolithography is defined as the product of the intensity of the light and the exposure time. If the intensity of the light was reduced by a factor of 10 and the exposure time was increased by a factor of 10, the dose will be the same. Therefore, I concluded that using longer exposure times would allow the intensity of the ultraviolet light through the chromium nanogap to be sufficient to perform nanolithography experiments.

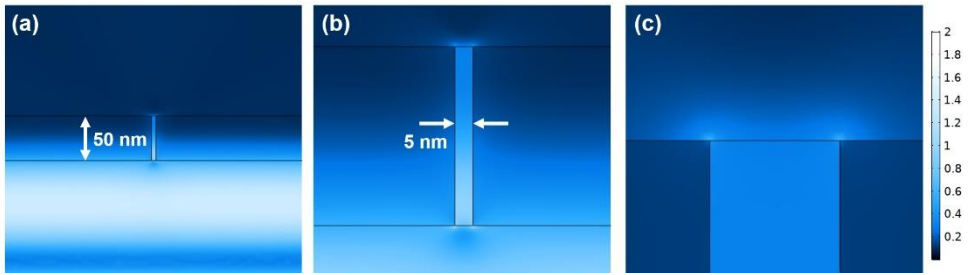


**Figure 3.3** Calculated electric field distribution by using the finite element method simulation.

### 3.3 Experimental details

Photolithography experiments were performed using conventional i-line mercury lamp in a mask aligner and chromium nanogaps. Firstly, I spin-coated a photoresist (AZ 5206-E, AZ Electronic Materials), diluted by a propylene glycol monomethyl ether acetate solvent (1:2 dilution). The thickness of the diluted photoresist on the silicon substrate was about 130 nm. Then, the 50-nm-thick chromium nanogap, which was attached to a blank mask, was contacted to the photoresist. Then I illuminated ultraviolet light using a mercury arc lamp in the mask aligner. The exposure time was 100 s. It should be noted that the thickness of the chromium layer was chosen to be 50 nm. It was because the chromium thickness below 50 nm could not block the ultraviolet light effectively. After the ultraviolet light illumination, I developed the photoresist sample by using AZ 500 MIF developer (AZ Electronic Materials). Then the sample was cleaned by deionized water and dried in nitrogen gas.

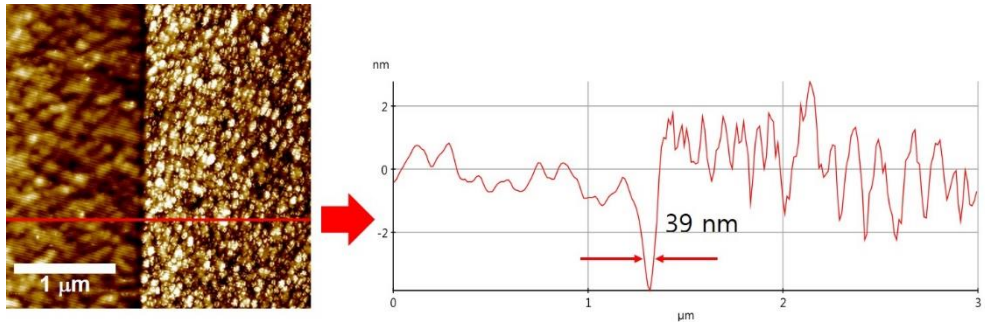
### 3.4 Resist development & lift-off images

Figure 3.4 showed the atomic force microscope image of the developed photoresist sample. The scan size of the sample was  $3\ \mu\text{m} \times 3\ \mu\text{m}$ . The black line at the center of the image in Figure 3.4 was the developed area. The width of the line was about 39 nm. Considering that the resolution of the conventional i-line photolithography was about  $1\ \mu\text{m}$ , this result was about 25 times better. It should be noted that the roughness of the photoresists in contact with 1st chromium layer and 2nd chromium layer was different from each other. This could occur in fabrication processes such as atomic layer deposition or chemical etching processes. This could occur in fabrication processes such as atomic layer deposition or chemical etching processes.

I also performed lift-off experiments. All the experimental processes were the same, but I used longer development time. After the development process, I deposited 20-nm-thick chromium metal by using electron beam evaporation (KVE-E2000, Korea Vacuum Tech) and removed the photoresist by using acetone and isopropanol. The final structures after the lift-off process were confirmed by the optical microscope and the scanning electron microscope. Figure 3.5(b) showed the square metal ring arrays on the silicon substrate, confirmed by the optical microscope. The chromium nanogap

photomask patterns were also shown in Figure 3.5(a). The mask pattern and lift-off patterns were similar, suggesting that the patterns were successfully transferred to the substrate. Using a scanning electron microscope, the linewidth of the transferred metal wire was checked. The averaged linewidth of the metal square ring arrays was about 220 nm, which was below the resolution limit of the conventional i-line photolithography. This result was about five times better than conventional photolithography.

The same experiment was attempted with thinner photoresist (thickness: 90 nm and 60 nm) for better feature size. I diluted the photoresist with different concentration (1:3 dilutions or 1:4 dilutions between the photoresist and propylene glycol monomethyl ether acetate solvent). However, due to the low verticality of the developed patterns, lift-off was largely unsuccessful.



**Figure 3.4** Atomic force microscope image of the developed photoresist.

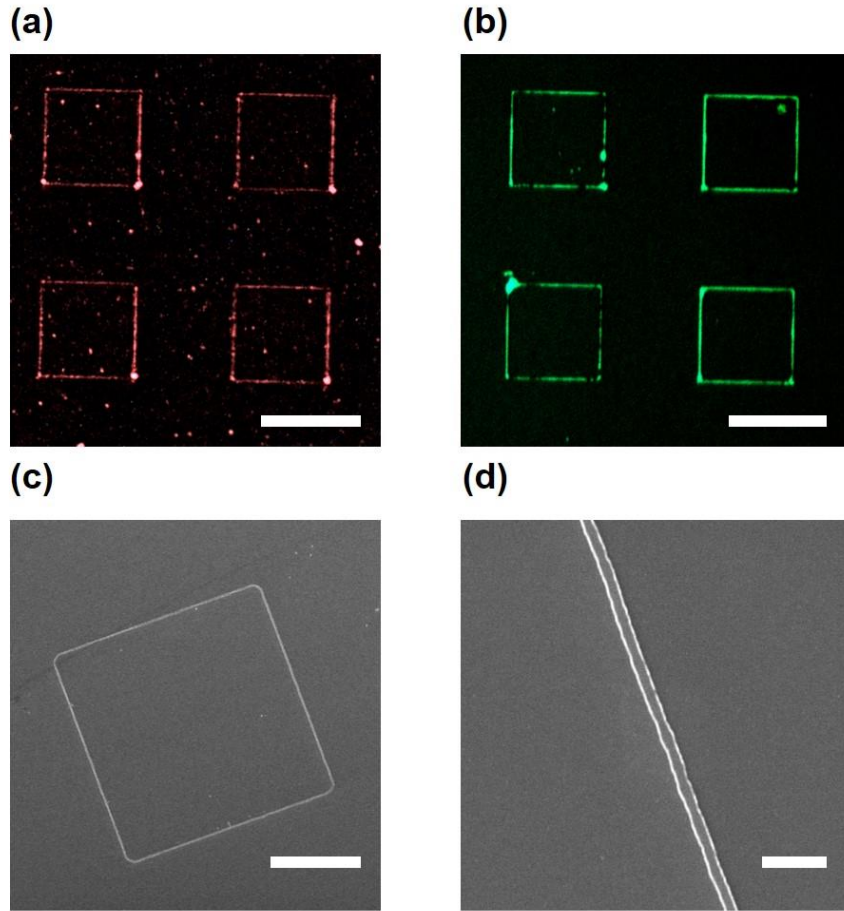


**Figure 3.5** (a) Dark-field optical microscope image of the chromium nanogap. (b) Optical microscope image of the patterned metal rings on a silicon substrate. (c) Scanning electron microscope image of the metal square ring. (d) Scanning electron microscope image of the metal wire. Scale bar: (a) 50  $\mu\text{m}$ ; (b) 50  $\mu\text{m}$ ; (c) 20  $\mu\text{m}$ ; (d) 2  $\mu\text{m}$ .

### 3.5 Conclusion

In conclusion, I have developed a cost-effective, straightforward method to make sub-10 nm feature chromium photomask. Chromium/aluminum/chromium trilayer could be made by conventional photolithography and lift-off technique, and then the dented-overhang structure could also be made by a simple wet etching process. This dented-overhang structure could prevent the sacrificial layer from being blocked by the second chromium deposition. The nanogap filled with aluminum oxide layer deposited by the atomic layer deposition method allowed me to make extremely long sub-10 nm feature slit arrays with large scale uniformity. Comparing previous atomic layer lithography methods, this method had several advantages. First, this method could bypass the mechanical exfoliation. It implied that one could choose the first and second metal layer without any restriction. In addition, this method could bypass the additional ion milling process, i.e. this method could reduce the total cost and time compared to the previous etching method. Unlike gold, silver, or copper nanogaps, the chromium nanogap could be used in the ultraviolet region. Therefore, my chromium nanogap would have a great potential for nanolithography, including plasmonic lithography, evanescent near-field optical lithography, etc.

# **Chapter 4. Terahertz-driven polymerization of resists in nanoantennas**

## **4.1 Introduction**

The surface plasmons in nanostructures could generate optical field enhancement, field confinement, local heating, and hot electron excitation. This allowed high-precision spatial control of photochemistry and increased the yield of chemical reactions. Therefore, various studies have been conducted for plasmon-induced chemistry, including photovoltaics [80] and photocatalysis [81]. In particular, many researchers have studied plasmon-induced polymerization for a number of applications, such as subwavelength lithography [17–19], near-field mapping [20–26], and spatial selective functionalization [28].

Despite these possible applications, the polymerization experiments using plasmonic nanostructures were limited. The wavelength of the light used in the previous experiments was limited from the ultraviolet to the near-infrared region. This was because the photon energy needed to polymerize the photoresist was in the ultraviolet region, and the surface plasmon in novel

metals could be excited in the visible to near-infrared light. The surface plasmon in nanostructure could make an optical near-field enhancement, therefore an intense light could be made in a small region. The intense light could induce multiphoton absorption in the photoresist, and cross-link the photoresist. However, there has been no report of cross-linking of the photoresist using longer wavelength light, such as mid-infrared or terahertz wave. It was because the probability of the chemical reactions decreased drastically as the number of the photons required for the polymerization increased. Then, can't we induce resist polymerization by using long-wavelength light?

Recently, some researchers have reported that strong field emission and hot electron emission can induce the resist (de)polymerization [29,82]. These experiments proved the possibility of a new way to resist polymerization. Therefore, if we can induce strong field emission or hot electron emission in nanoscale, we can demonstrate nanoscale resist polymerization with long-wavelength light.

Here, I used intense terahertz light and terahertz-resonant nanoantenna structures to induce strong field emission of electrons. These electrons were used to cross-link the photoresist near the nanoantennas, demonstrating the terahertz-driven polymerization.

## 4.2 Terahertz wave & terahertz time-domain spectroscopy

Terahertz wave is an electromagnetic wave having a frequency of about 0.1 THz to 10 THz. (Figure 4.1) The order of the photon energy of the terahertz wave is about meV and is much smaller than molecular electronic transition energy. Instead, the photon energies of the terahertz wave correspond to intermolecular interactions [83–87] and superconducting energy gaps [88]. Therefore, the terahertz spectroscopy can have great potential to be used in non-destructive inspection [89,90], spectroscopy in a biological system [91,92] or strongly-correlated systems [93].

Recently, various terahertz generation and detection techniques were developed, including a photoconductive antenna [94] and optical rectification [95] method. In these methods, the terahertz signal was detected in the time domain, and these techniques were therefore referred to as “terahertz-time domain spectroscopy”.

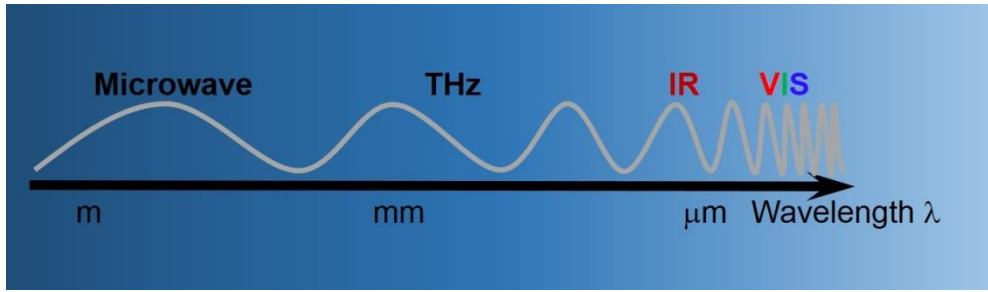
Meanwhile, in the terahertz regime, noble metals such as gold or silver can be approximated as perfect conductors, since their plasma frequency is much higher than the frequency of interests [2]. Even though the terahertz wave cannot excite surface plasmons in noble metals, this is extremely useful to confine terahertz electromagnetic

waves in the metallic nanogap, since the refractive index of the metal is huge [2] (Figure 4.2). Therefore, terahertz–time domain spectroscopy is a useful tool to investigate the extreme physics in metallic nanogap, enabling to see the new phenomena.

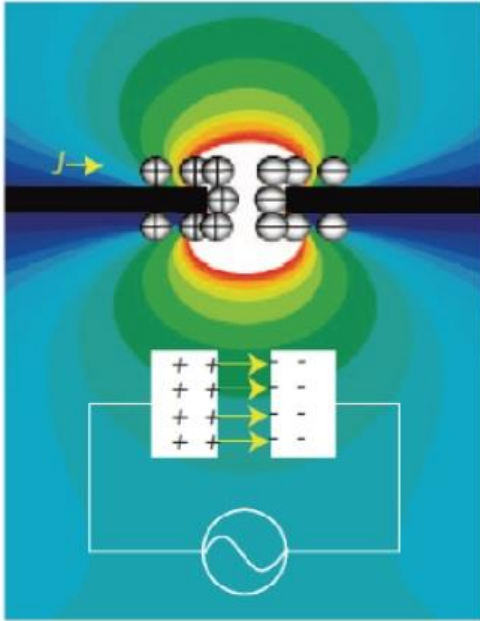
I performed terahertz time–domain spectroscopy by using femtosecond oscillator– and regenerative amplifier–based terahertz system.

Figure 4.3 showed the schematics of femtosecond Ti: Sapphire laser–based terahertz time–domain spectroscopy system. The femtosecond laser beam had 780 nm center wavelength, 80 MHz repetition rate, and 130 fs pulse width (Mira 900 and Verdi V5, Coherent). The laser beam was divided into pump and probe beam. Then the pump beam and biased GaAs photoconductive emitter were used to generate single–cycle terahertz pulses. Off–axis parabolic mirrors (NA=0.25) were used to focus the terahertz pulses, and the pulses were incident normally in the sample. Transmitted terahertz wave from the sample was collected by another parabolic mirrors (NA=0.32) and detected by using electro–optic sampling method. For electro–optic sampling, I used (110)–oriented ZnTe crystal. In the experiments, the substrate side was illuminated by the incoming terahertz wave. The terahertz signal from the sample was normalized by the terahertz signal from the substrate.

For terahertz-driven polymerization experiments, I used amplifier-based, high-power terahertz system. Figure 4.4 showed the schematics of the high-power terahertz system. I used optical rectification using tilted-pulse-front to generate intense terahertz wave. A prism-cut lithium niobate crystal and femtosecond pulses from Ti: Sapphire regenerate amplifier (repetition rate: 1 KHz) were used here. The maximum terahertz electric field was about 400 kV/cm at the center of the focal point in the air. The transmitted terahertz waves from the samples were collected by parabolic mirrors and detected by the electro-optic sampling method using (110) oriented ZnTe crystal. The peak frequency of the generated terahertz wave was 0.8 THz. The incoming terahertz wave illuminates the sample side first. All experiments were performed at room temperature and ambient pressure.



**Figure 4.1** The terahertz wave lies between the infrared light and the microwave.



**Figure 4.2** Concept of the confined terahertz electromagnetic waves in the metallic nanogap.

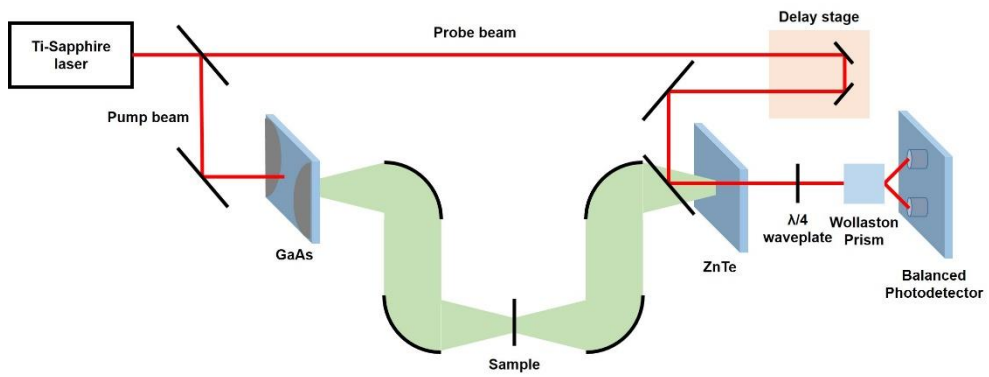


**Figure 4.3** Schematics of the oscillator-based, time-domain terahertz spectroscopy setup.

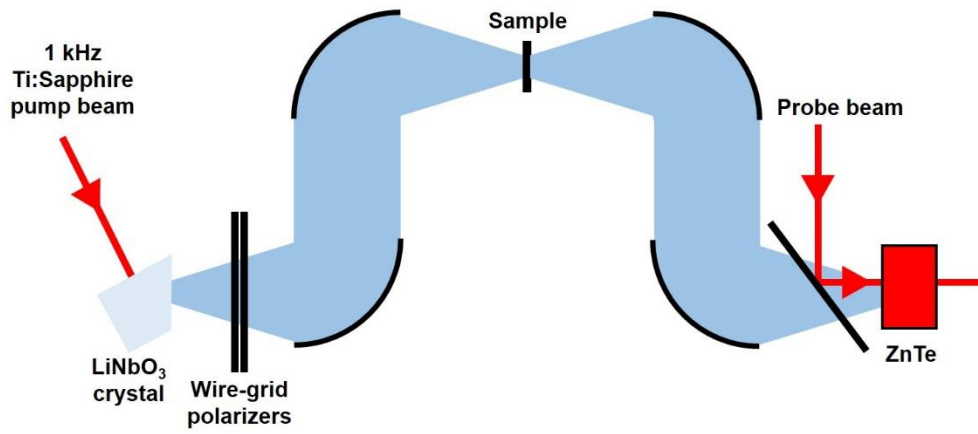


Figure 4.4 Schematics of the high-power terahertz generation by optical rectification using the tilted-pulse-front.

### 4.3 Kirchhoff integral formalism

I used Kirchhoff integral formalism to experimentally estimate the terahertz electric field enhancement factor [96]. The enhanced electric field near the subwavelength aperture was related to the amplitude of the transmitted far-field (Figure 4.5). The far field at the detection point in the normal to the sample was given by the Kirchhoff integral,

$$\mathbf{E}_{\text{far}} = \frac{e^{ikr}}{i\lambda r} \int_{\text{screen}} \mathbf{E}_{\text{near}}(\mathbf{r}') da' \quad (4.1)$$

where  $\mathbf{E}_{\text{far}}$  is the electric far field,  $k$  is the electromagnetic wavevector,  $\lambda$  is the wavelength,  $\mathbf{E}_{\text{near}}$  is the electric near field,  $\mathbf{r}$  is the observation point far from the apertures. In this equation, the electric far-field at the detection point could be calculated from the electric near-field on the screen. In our terahertz nanogap experiment, the detected signal could be given by

$$\begin{aligned} E_{\text{sample}} &\propto \int_{\text{screen}} E_{\text{near}} da' \\ &= \int_{\text{aperture}} E_{\text{gap}} da' \cong \langle E_{\text{gap}} \rangle \times (\text{gap area}) \end{aligned} \quad (4.2)$$

Also, the signal from the bare substrate could be given by

$$E_{\text{reference}} \propto \int_{\text{spot}} E_0 da' = E_0 \times (\text{spot size}) \quad (4.3)$$

where  $\langle E_{\text{gap}} \rangle$  means the averaged electric near-field over the slit

area. In equation (4.2), I assumed that the direct transmission through the metal could be ignored and the electric field distribution inside the gap was constant over the area. Finally, the electric near-field enhancement factor could be calculated as

$$\left| \frac{E_{\text{gap}}}{E_0} \right| = \frac{1}{\beta} \frac{E_{\text{sample}}}{E_{\text{reference}}} \quad (4.4)$$

where  $\beta$  is the coverage ratio of the sample.

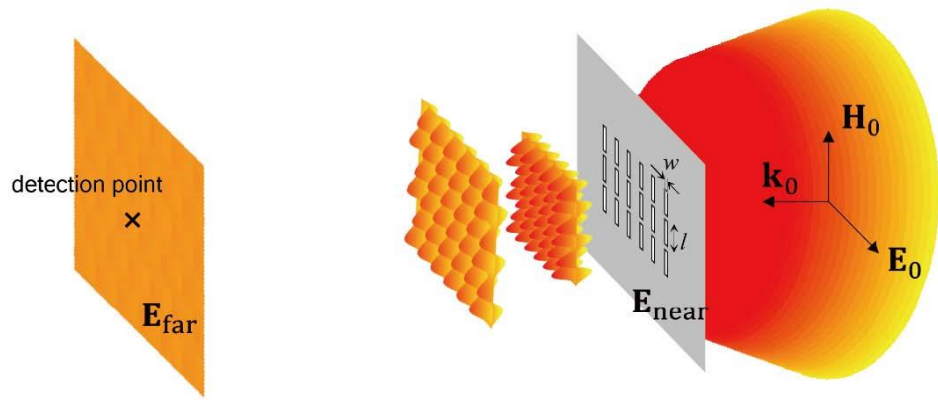


**Figure 4.5** Schematics of a diffraction geometry of slit arrays in a metallic screen.

## 4.4 Experimental details and results

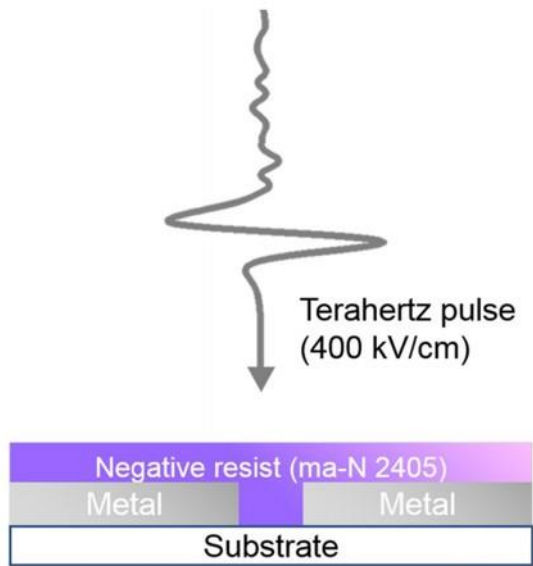
Figure 4.6 showed the schematics of terahertz-driven polymerization experiments. A negative tone photoresist ma-N 2405 (Microchem) was spin-coated onto the terahertz nanoantenna samples (4000 rpm, 1 min). The terahertz nanoantennas were made by above-mentioned methods – focused ion beam or electron beam lithography. The thickness of the photoresist ma-N 2405 was about 500 nm, which was thick enough to cover the entire samples. The sample was baked at 90 °C for 150 s. The ma-N 2405 photoresist was a compound of aromatic bisazide and phenolic resin (novolak). Each was a photoactive compound and a polymeric bonding agent, respectively. Note that the photoresist was not chemically amplified[97]. The development process was carried out using ma-D 525 developers (Microchem) after terahertz illumination. This developer was composed of tetramethylammonium hydroxide in aqueous solution.

Figure 4.7 showed the results of the terahertz-driven polymerization in nano-slot antennas. In these experiments, the high-power terahertz pulses were applied to the samples for two hours. The polarization direction of the terahertz pulses was perpendicular to the long axis of the nano-slot antenna. To prevent the effect of the ultraviolet light from outside, the experiments were

performed in dark ambient condition. As can be seen in Figure 4.7 (a), the photoresist polymerization occurred only inside the gap. There was no photoresist on the metal. It implied that the terahertz near-field inside the gap was an important factor for the resist polymerization. Nevertheless, the enhanced terahertz near-field itself could not be the origin of the resist polymerization, since the photon energy of the terahertz light was the only order of meV. Even though the terahertz light was focused into the deep subwavelength region, the probability to induce the multiphoton absorption was too small. Therefore, I assumed that the polymerization was induced not by the multiphoton absorption, but by the strong field emission of electrons.

To confirm the hypothesis, I fabricated bowtie-shaped terahertz nanoantenna. Figure 4.8 showed the scanning electron microscope image of the terahertz-resonant bowtie nanoantenna. I performed the same experiments as that performed in the slot antenna sample and obtained the polymerized photoresist at the center of the bowtie antenna where giant field confinement and enhancement occurred. Figure 4.8(b) showed the cross-linked photoresist at the center of the antenna. We could confirm that the strong field emission of the electron was the main origin of the resist polymerization, as we will discuss in the next section.

To see the near-field distribution, or electron emission distribution, I fabricated squared-shaped, terahertz resonant nano-slot antenna. Figure 4.10(a) showed the scanning electron microscope image of the sample. Firstly, to investigate the properties of this antenna, terahertz-time domain spectroscopy was performed by using the oscillator-based system, as mentioned in previous sections. In addition, the terahertz field enhancement factor was calculated from the experimental data and Kirchhoff integral formalism[96]. The normalized amplitude was about 0.03 at 0.8 THz (resonance frequency), and the corresponding field enhancement factor was about 100 (Figure 4.9). In these experiments, I illuminated the intense terahertz pulses to the sample for four hours. After the development process, the photoresist could be observed both inside and outside the gap. The photoresist could be observed only on the side perpendicular to the terahertz polarization direction. The shape of the remaining photoresist was similar to the terahertz near-field distribution in the nano-slot antenna[5]. Figure 4.10(b) showed the shape of the remaining photoresists near the square-shaped nano-slot antenna. Since the field emission of electrons was strongly related to the terahertz near-field enhancement factor, the terahertz-driven polymerization could map the local near-field distribution.



**Figure 4.6** Schematics of high-power terahertz wave illumination to the photoresist/metal nano-slot antenna sample.

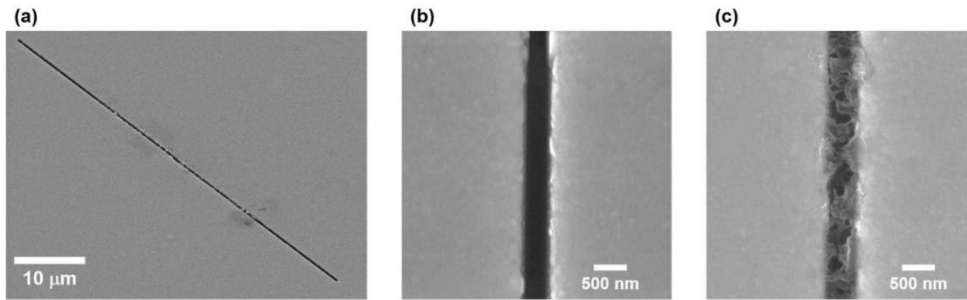


**Figure 4.7** Terahertz wave-assisted resist polymerization in nano-slot antenna. (a) The photoresist was cross-linked at the center of the terahertz nano-slot antenna. (b) scanning electron microscope image of the nano-slot antenna before the photoresist coating. (c) scanning electron microscope image of the nano-slot antenna after the high power terahertz wave illumination and the photoresist polymerization.

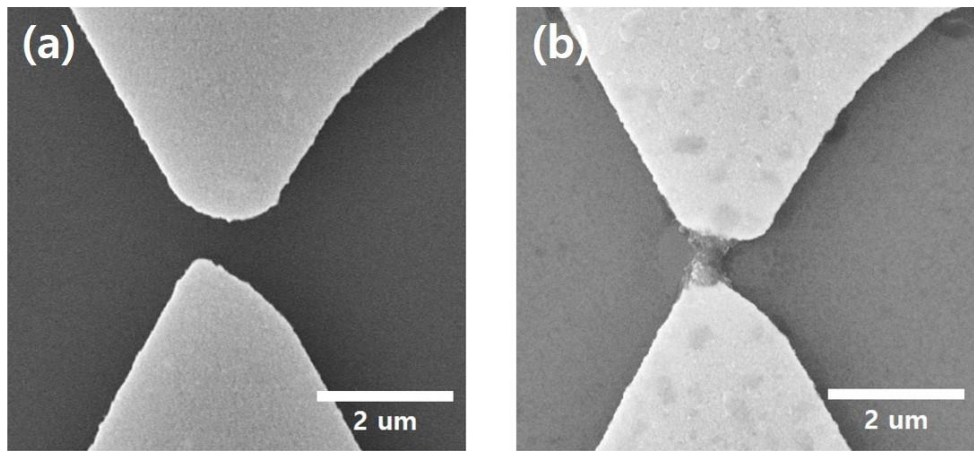


**Figure 4.8** Terahertz wave–assisted resist polymerization in bowtie nanoantenna. (a) scanning electron microscope image of the terahertz–resonant bowtie nanoantenna before photoresist coating. (b) scanning electron microscope image of the bowtie nanoantenna after the high power terahertz wave illumination and the photoresist polymerization.

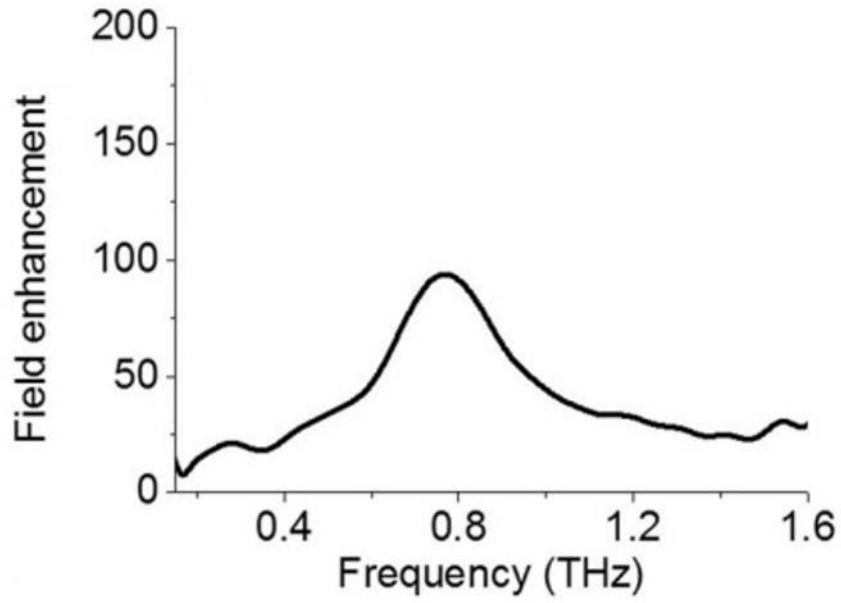


**Figure 4.9** Measured field enhancement factor of the square-shaped nano-slot antenna depending on the frequencies.

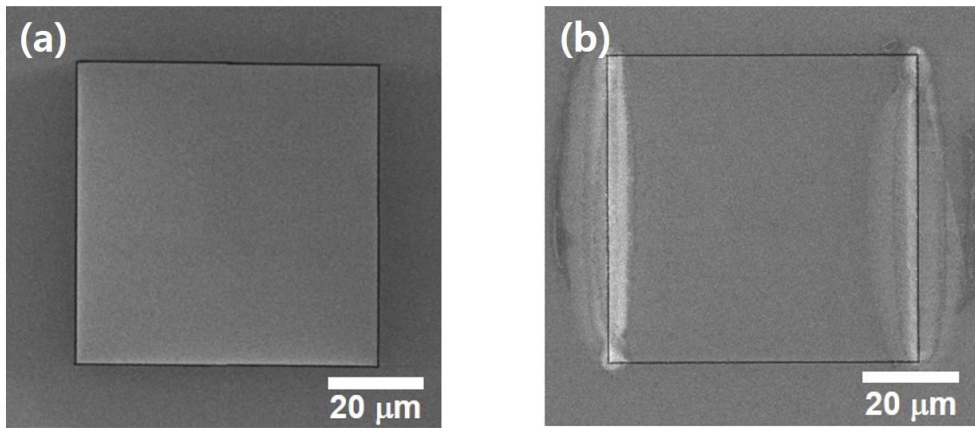


**Figure 4.10** Terahertz wave-assisted resist polymerization in squared-shaped terahertz nano-slot antenna. (a) scanning electron microscope image of the square-shaped nano-slot antenna before the photoresist coating. (b) scanning electron microscope image of the square-shaped nano-slot antenna after the high power terahertz wave illumination and the photoresist polymerization.

## 4.5 Finite element method simulation

I performed finite element method simulation by using COMSOL Multiphysics 5.3 software, to see the terahertz field enhancement factor at the center of the bowtie nanoantenna. The simulated terahertz electric field distribution is shown in Figure 4.11. In this simulation, the size of the antenna gap was  $1\mu\text{m}$ , to match with the real samples. The thickness of the metal was 100 nm, and it was approximated to the perfect metal. The size of the bowtie antenna in the simulation was same as the experimental one: the period of the antennas was  $360\mu\text{m}$ , the length of the long axis was  $170\mu\text{m}$ , and the length of the short axis was  $85\mu\text{m}$ , respectively. The field enhancement factor at the center of the bowtie antenna reached  $\sim 300$ .

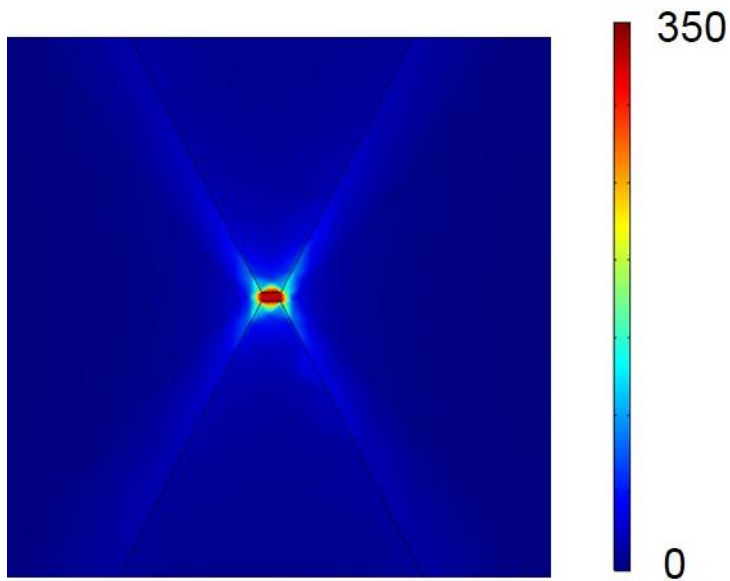


**Figure 4.11** Calculated electric field distribution in the terahertz-resonant bowtie nanoantenna by using the finite element method simulation.

## 4.6 Tunneling current measurement

I measured the tunneling currents between the two poles of the bowtie antennas while illuminating the intense terahertz pulses to the sample. Since the poles were isolated, I could measure the electric currents by using the probe station[98]. In the measurement, I used a 1  $\mu\text{m}$  gap bowtie antenna. I illuminated the intense terahertz wave to the substrate side first. The intensity of the terahertz wave was adjusted to the two wire grid polarizers to fix the polarization direction. Figure 4.12 showed the measured electric current depending on the amplitude of the incident terahertz wave. I observed that the electric current was increased exponentially when the amplitude of the terahertz electric field increased. I analyzed the electric current data by using Fowler–Nordheim plot and obtained a linear graph (Figure 4.12(b)). I also plotted the theoretical electric current using the Fowler–Nordheim equation and the result of the terahertz field enhancement factor in the finite element method simulation[99]. In the finite element simulation, the terahertz field enhancement factor was about 300 at the resonant frequency. In the Fowler–Nordheim equation, the field emission current density  $J$  is given by the form [100]

$$J = \alpha_M \lambda_C a (\beta E_0)^2 \Phi^{-1} \exp \left\{ -\frac{vb\Phi^{3/2}}{\beta E_0} \right\},$$

where  $a = 1.53 \times 10^{-6} \text{ AeV}^{-2}$  and  $b = 6.829 \times 10^9 \text{ eV}^{-\frac{3}{2}} \text{Vm}^{-1}$ , are first and second Fowler–Nordheim constants, respectively,  $\alpha_M$  is the area efficiency of emission,  $\lambda_C$  is a characteristic supply correction factor,  $\nu$  is a correction factor associated with the barrier shape,  $\Phi$  is the work function of the metal (gold),  $\beta$  is the field enhancement factor, and  $E_0$  is the incident electric field. In our case, the barrier shape is triangular, so the factor  $\alpha_M \lambda_C \nu$  becomes  $\alpha_M = \lambda_C = \nu = 1$  [100].

In Figure 4.12, I plotted the theoretical data in the red line. Surprisingly, the theoretical and experimental data were in good agreement with each other. In the Fowler–Nordheim plot (Figure 4.12(b)), the slope was determined by the factor  $-\nu b \Phi^{3/2} / \beta$ , i.e. the field enhancement factor  $\beta$ . That is, the field enhancement factor calculated by the finite element method simulation and the experimental data were in good agreement with each other. By using this graph, I was also able to calculate the electron dose. The electron dose is defined by the simple formula

$$D = \frac{T \times I}{A}$$

where T is exposure time, I is the electric current of the electron beam, and A is the exposed area. In this experiment, the exposure time was two hours. The calculated electron doses were shown in

Figure 4.12(a). In our experiments, the doses were about  $10^5 \sim 10^6$  electrons/nm<sup>2</sup>. Generally, the amount of doses needed in high-dose electron beam lithography is  $> 10^4$  electrons/nm<sup>2</sup>. In our experiments, the doses were much higher than that of the conventional high-dose electron beam lithography, which implies that our experimental system is indeed able to polymerize the photoresist. The doses were similar to the previous report in the terahertz-micron gap ( $10^6$  electrons/nm<sup>2</sup>) [82], but the doses were much higher than that of the previous reports using a femtosecond laser ( $10^4 \sim 10^5$  electrons/nm<sup>2</sup>) [29]. In terms of the current density, however, the femtosecond one is much higher than the terahertz one. It is because the enhanced optical electric field of the femtosecond laser ( $\sim 25$  V/nm) was much higher than the enhanced terahertz electric field ( $\sim 12$  V/nm) [29,82].

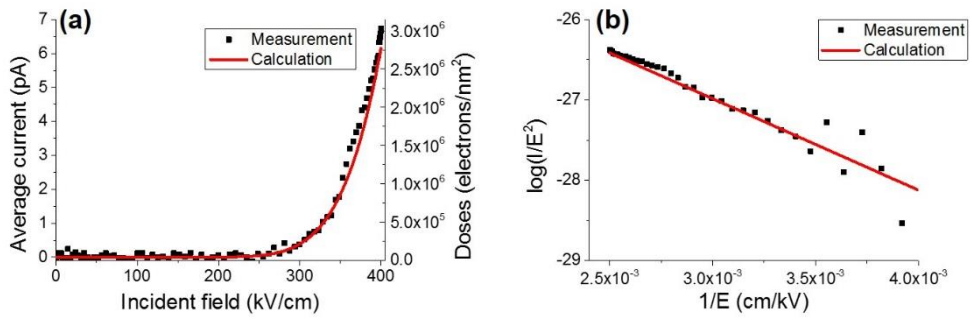


**Figure 4.12** (a) Measured/calculated electric current depending on the incident terahertz field amplitude. (b) Fowler–Nordheim plot of the measured/calculated electric current.

## 4.7 Conclusion

In conclusion, I demonstrated terahertz-field-assisted polymerization of photoresists in nanoantennas. The photoresists near the terahertz hot-spot were cross-linked. The enhanced terahertz electric field induced strong-field emission from the metallic antennas, and the electrons from the metal made the photoresist polymerized. The electric current measurement, simulation, and the theoretical calculation of the current density were consistent with each other, indicating that the terahertz-driven polymerization was originated from the electron emission, not multiphoton absorption. The terahertz-driven polymerization has shown a new possibility that the long-wavelength light can also be used in nanochemistry.

## **Chapter 5. Conclusion**

In this thesis, the interaction between the light and metallic nanogap was discussed and the application of this interaction as a photoresist polymerization was also discussed. The metallic nanogap was fabricated using various methods, including atomic layer lithography, electron beam lithography, and focused ion beam technique. Then the optical field distribution of the ultraviolet light or the terahertz wave near the nanogap was demonstrated by the finite element method simulation, to confirm the strong optical field confinement near the nanogap. This strong field confinement was used to cross-link the photoresist near the nanogap experimentally, by using the absorption of the ultraviolet light or strong field emission of electrons from the metal. This work would provide new applications of the nanogap structures as a platform of nano-photochemistry.

# Bibliography

- [1] T. W. Ebbesen, H. J. Lezec, H. F. Ghaemi, T. Thio, and P. A. Wolff, *Nature* **391**, 667 (1998).
- [2] M. A. Seo *et al.*, *Nat. Photonics* **3**, 152 (2009).
- [3] J. H. Kang, D. S. Kim, and Q. H. Park, *Phys. Rev. Lett.* **102**, 093906 (2009).
- [4] F. J. Garcia-Vidal, E. Moreno, J. A. Porto, and L. Martin-Moreno, *Phys. Rev. Lett.* **95**, 103901 (2005).
- [5] X. Chen *et al.*, *Nat. Commun.* **4**, 2361 (2013).
- [6] Y. M. Bahk *et al.*, *Phys. Rev. Lett.* **115**, 125501 (2015).
- [7] Y. M. Bahk, S. Han, J. Rhie, J. Park, H. Jeon, N. Park, and D. S. Kim, *Phys. Rev. B* **95**, 075424 (2017).
- [8] T. Kang, J. Rhie, J. Park, Y. M. Bahk, J. S. Ahn, H. Jeon, and D. S. Kim, *Appl. Phys. Express* **8**, 092003 (2015).
- [9] J. S. Ahn, T. Kang, D. K. Singh, Y. M. Bahk, H. Lee, S. B. Choi, and D. S. Kim, *Opt. Express* **23**, 4897 (2015).
- [10] K. Lee *et al.*, *ACS Photonics* **3**, 537 (2016).
- [11] O. K. Suwal, J. Rhie, N. Kim, and D. S. Kim, *Sci. Rep.* **7**, 45638 (2017).
- [12] J. Y. Kim, B. J. Kang, J. Park, Y. M. Bahk, W. T. Kim, J. Rhie, H. Jeon, F. Rotermund, and D. S. Kim, *Nano Lett.* **15**, 6683

(2015).

- [13] S. Han *et al.*, ACS Photonics **3**, 1440 (2016).
- [14] T. Kang, R. H. J. Y. Kim, G. Choi, J. Lee, H. Park, H. Jeon, C. H. Park, and D. S. Kim, Nat. Commun. **9**, 4914 (2018).
- [15] H. B. Cai, Y. K. Wu, Y. M. Dai, N. Pan, Y. C. Tian, Y. Luo, and X. P. Wang, Opt. Express **24**, 20808 (2016).
- [16] D. Yoo *et al.*, Nano Lett. **18**, 1930 (2018).
- [17] W. Srituravanich, N. Fang, C. Sun, Q. Luo, and X. Zhang, Nano Lett. **4**, 1085 (2004).
- [18] A. Sundaramurthy, P. J. Schuck, N. R. Conley, D. P. Fromm, G. S. Kino, and W. E. Moerner, Nano Lett. **6**, 355 (2006).
- [19] K. Ueno, S. Takabatake, Y. Nishijima, V. Mizeikis, Y. Yokota, and H. Misawa, J. Phys. Chem. Lett. **1**, 657 (2010).
- [20] N. Murazawa, K. Ueno, V. Mizeikis, S. Juodkazis, and H. Misawa, J. Phys. Chem. C **113**, 1147 (2009).
- [21] T. Geldhauser, S. Ikegaya, A. Kolloch, N. Murazawa, K. Ueno, J. Boneberg, P. Leiderer, E. Scheer, and H. Misawa, Plasmonics **6**, 207 (2011).
- [22] K. G. Stamplecoskie, N. L. Pacioni, D. Larson, and J. C. Scaiano, J. Am. Chem. Soc. **133**, 9160 (2011).
- [23] C. Deeb, X. Zhou, R. Miller, S. K. Gray, S. Marguet, J. Plain, G. P. Wiederrecht, and R. Bachelot, J. Phys. Chem. C **116**, 24734

- (2012).
- [24] T. Geldhauser, A. Kolloch, N. Murazawa, K. Ueno, J. Boneberg, P. Leiderer, E. Scheer, and H. Misawa, *Langmuir* **28**, 9041 (2012).
- [25] G. Volpe, M. Noack, S. S. Acimovic, C. Reinhardt, and R. Quidant, *Nano Lett.* **12**, 4864 (2012).
- [26] C. Gruber, A. Hirzer, V. Schmidt, A. Trugler, U. Hohenester, H. Ditlbacher, A. Hohenau, and J. R. Krenn, *Appl. Phys. Lett.* **106** (2015).
- [27] T. Ding, J. Mertens, A. Lombardi, O. A. Scherman, and J. J. Baumberg, *ACS Photonics* **4**, 1453 (2017).
- [28] X. Zhou *et al.*, *ACS Photonics* **2**, 121 (2015).
- [29] R. G. Hobbs, W. P. Putnam, A. Fallahi, Y. J. Yang, F. X. Kartner, and K. K. Berggren, *Nano Lett.* **17**, 6069 (2017).
- [30] J. Lee, S. Mubeen, X. L. Ji, G. D. Stucky, and M. Moskovits, *Nano Lett.* **12**, 5014 (2012).
- [31] S. C. Warren and E. Thimsen, *Energy Environ. Sci.* **5**, 5133 (2012).
- [32] A. Sheikh, A. Yengantiwar, M. Deo, S. Kelkar, and S. Ogale, *Small* **9**, 2091 (2013).
- [33] Z. H. Zhang, L. B. Zhang, M. N. Hedhili, H. N. Zhang, and P. Wang, *Nano Lett.* **13**, 14 (2013).

- [34] M. Valenti, D. Dolat, G. Biskos, A. Schmidt–Ott, and W. A. Smith, *J. Phys. Chem. C* **119**, 2096 (2015).
- [35] L. W. Zhang, L. O. Herrmann, and J. J. Baumberg, *Sci. Rep.* **5**, 16660 (2015).
- [36] P. Zhang, T. Wang, and J. L. Gong, *Adv. Mater.* **27**, 5328 (2015).
- [37] C. J. Chen, C. K. Chen, T. H. Lu, S. F. Hu, and R. S. Liu, *RSC Adv.* **6**, 103160 (2016).
- [38] D. Y. Hu, P. Diao, D. Xu, and Q. Y. Wu, *Nano Res.* **9**, 1735 (2016).
- [39] K. K. Patra and C. S. Gopinath, *ChemCatChem* **8**, 3294 (2016).
- [40] M. Valenti, M. P. Jonsson, G. Biskos, A. Schmidt–Ott, and W. A. Smith, *J. Mater. Chem. A* **4**, 17891 (2016).
- [41] M. Valenti, E. Kontoleta, I. A. Digdaya, M. P. Jonsson, G. Biskos, A. Schmidt–Ott, and W. A. Smith, *ChemNanoMat* **2**, 739 (2016).
- [42] C. W. Moon, S. Y. Lee, W. Sohn, D. M. Andoshe, D. H. Kim, K. Hong, and H. W. Jang, *Part. Part. Syst. Charact.* **34**, 1600340 (2017).
- [43] A. Naldoni *et al.*, *Adv. Opt. Mater.* **5**, 1601031 (2017).
- [44] S. Mukherjee *et al.*, *Nano Lett.* **13**, 240 (2013).
- [45] L. Zhou *et al.*, *Nano Lett.* **16**, 1478 (2016).

- [46] S. Mukherjee, L. A. Zhou, A. M. Goodman, N. Large, C. Ayala–Orozco, Y. Zhang, P. Nordlander, and N. J. Halas, *J. Am. Chem. Soc.* **136**, 64 (2014).
- [47] L. N. Tripathi, T. Kang, Y. M. Bahk, S. Han, G. Choi, J. Rhie, J. Jeong, and D. S. Kim, *Opt. Express* **23**, 14937 (2015).
- [48] H. Yang, D. S. Kim, R. H. J. Y. Kim, J. S. Ahn, T. Kang, J. Jeong, and D. Lee, *Sci. Rep.* **8**, 2751 (2018).
- [49] J. Jeong, J. Rhie, W. Jeon, C. S. Hwang, and D. S. Kim, *J. Infrared Millim. Te.* **36**, 262 (2015).
- [50] Y. G. Jeong *et al.*, *Nano Lett.* **15**, 6318 (2015).
- [51] S. Han, Y. M. Bahk, N. Park, and D. S. Kim, *Opt. Express* **24**, 2065 (2016).
- [52] J. Y. Kim *et al.*, *Sci. Rep.* **6**, 29103 (2016).
- [53] S. J. Park, T. Y. Kim, C. H. Park, and D. S. Kim, *Sci. Rep.* **6**, 22981 (2016).
- [54] L. N. Tripathi, Y. M. Bahk, G. Choi, S. Han, N. Park, and D. S. Kim, *Appl. Phys. Express* **9**, 032001 (2016).
- [55] G. Choi, Y. M. Bahk, T. Kang, Y. Lee, B. H. Son, Y. H. Ahn, M. Seo, and D. S. Kim, *Nano Lett.* **17**, 6397 (2017).
- [56] J. Jeong, D. Kim, H. R. Park, T. Kang, D. Lee, S. Kim, Y. M. Bahk, and D. S. Kim, *Nanophotonics* **7**, 347 (2018).
- [57] J. Jeong, H. S. Yun, D. Kim, K. S. Lee, H. K. Choi, Z. H. Kim,

- S. W. Lee, and D. S. Kim, *Adv. Opt. Mater.* **6**, 1800582 (2018).
- [58] D. Kim, J. Jeong, G. Choi, Y. M. Bahk, T. Kang, D. Lee, B. Thusa, and D. S. Kim, *ACS Photonics* **5**, 1885 (2018).
- [59] N. Kim, S. In, D. Lee, J. Rhie, J. Jeong, D. S. Kim, and N. Park, *ACS Photonics* **5**, 278 (2018).
- [60] J. Rhie, D. Lee, Y. M. Bahk, J. Jeong, G. Choi, Y. Lee, S. Kim, S. Hong, and D. S. Kim, *J. Micro/Nanolith. MEMS MOEMS* **17**, 023504 (2018).
- [61] H. S. Yun, J. Jeong, D. Kim, and D. S. Kim, *Adv. Opt. Mater.* **7**, 1800856 (2019).
- [62] A. A. Tseng, K. Chen, C. D. Chen, and K. J. Ma, *IEEE T. Electron. Pack.* **26**, 141 (2003).
- [63] H. Schiff, *J. Vac. Sci. Technol. B* **26**, 458 (2008).
- [64] R. Garcia, R. V. Martinez, and J. Martinez, *Chem. Soc. Rev.* **35**, 29 (2006).
- [65] C. W. Gwyn, R. Stulen, D. Sweeney, and D. Attwood, *J. Vac. Sci. Technol. B* **16**, 3142 (1998).
- [66] S. Y. Lee, H. J. Kim, J. Ahn, I. Y. Kang, and Y. C. Chung, *J. Korean Phys. Soc.* **41**, 427 (2002).
- [67] N. Mojarad, J. Gobrecht, and Y. Ekinici, *Sci. Rep.* **5**, 9235 (2015).
- [68] M. D. Levenson, N. S. Viswanathan, and R. A. Simpson, *IEEE*

- T. Electron. Dev. **29**, 1828 (1982).
- [69] L. P. Ghislain, V. B. Elings, K. B. Crozier, S. R. Manalis, S. C. Minne, K. Wilder, G. S. Kino, and C. F. Quate, Appl. Phys. Lett. **74**, 501 (1999).
- [70] M. Switkes and M. Rothschild, J. Vac. Sci. Technol. B **19**, 2353 (2001).
- [71] J. Finders, M. Dusa, B. Vleeming, B. Hepp, M. Maenhoudt, S. Cheng, and T. Vandeweyer, J. Micro/Nanolith. MEMS MOEMS **8**, 011002 (2009).
- [72] M. M. Alkaisi, R. J. Blaikie, S. J. McNab, R. Cheung, and D. R. S. Cumming, Appl. Phys. Lett. **75**, 3560 (1999).
- [73] R. J. Blaikie, M. M. Alkaisi, S. J. McNab, D. R. S. Cumming, R. Cheung, and D. G. Hasko, Microelectron. Eng. **46**, 85 (1999).
- [74] D. B. Shao and S. C. Chen, Appl. Phys. Lett. **86** (2005).
- [75] Y. Kim, S. Kim, H. Jung, E. Lee, and J. W. Hahn, Opt. Express **17**, 19476 (2009).
- [76] L. Pan *et al.*, Sci. Rep. **1**, 175 (2011).
- [77] J. J. Dong, J. Liu, G. G. Kang, J. H. Xie, and Y. T. Wang, Sci. Rep. **4**, 5618 (2014).
- [78] N. Fang, H. Lee, C. Sun, and X. Zhang, Science **308**, 534 (2005).
- [79] P. B. Johnson and R. W. Christy, Phys. Rev. B **9**, 5056 (1974).

- [80] H. A. Atwater and A. Polman, *Nat. Mater.* **9**, 205 (2010).
- [81] X. M. Zhang, Y. L. Chen, R. S. Liu, and D. P. Tsai, *Rep. Prog. Phys.* **76**, 046401 (2013).
- [82] S. L. Lange, T. M. B. Kristensen, K. Iwaszczuk, and P. U. Jepsen, in *2017 42nd International Conference on Infrared, Millimeter, and Terahertz Waves (IRMMW–THz)* (2017).
- [83] M. Vanexter, C. Fattinger, and D. Grischkowsky, *Opt. Lett.* **14**, 1128 (1989).
- [84] H. Harde and D. Grischkowsky, *J. Opt. Soc. Am. B* **8**, 1642 (1991).
- [85] H. Harde, S. Keiding, and D. Grischkowsky, *Phys. Rev. Lett.* **66**, 1834 (1991).
- [86] M. Hangyo, M. Tani, and T. Nagashima, *Int. J. Infrared Milli.* **26**, 1661 (2005).
- [87] P. U. Jepsen, D. G. Cooke, and M. Koch, *Laser Photonics Rev.* **5**, 124 (2011).
- [88] S. L. Norman, *Phys. Rev.* **167**, 393 (1968).
- [89] D. Zimdars, J. S. White, G. Stuk, A. Chernovsky, G. Fichter, and S. Williamson, *Insight* **48**, 537 (2006).
- [90] I. Amenabar, F. Lopez, and A. Mendikute, *J. Infrared Millim. Te.* **34**, 152 (2013).
- [91] E. Pickwell and V. P. Wallace, *J. Phys. D* **39**, R301 (2006).

- [92] X. Yang, X. Zhao, K. Yang, Y. P. Liu, Y. Liu, W. L. Fu, and Y. Luo, Trends Biotechnol. **34**, 810 (2016).
- [93] N. Kida, H. Murakami, and M. Tonouchi, Terahertz Optics in Strongly Correlated Electron Systems, edited by K. Sakai, Terahertz Optoelectronics, Topics in Applied Physics, **97**, Springer, Berlin, Heidelberg.
- [94] P. U. Jepsen, R. H. Jacobsen, and S. R. Keiding, J. Opt. Soc. Am. B **13**, 2424 (1996).
- [95] X. C. Zhang, Y. Jin, and X. F. Ma, Appl. Phys. Lett. **61**, 2764 (1992).
- [96] J. S. Kyoung, M. A. Seo, H. R. Park, K. J. Ahn, and D. S. Kim, Opt. Commun. **283**, 4907 (2010).
- [97] H. Elsner, H. G. Meyer, A. Voigt, and G. Grutzner, Microelectron. Eng. **46**, 389 (1999).
- [98] M. Buret *et al.*, Nano Lett. **15**, 5811 (2015).
- [99] R. H. Fowler and L. Nordheim, Proc. R. Soc. Lond. A **119**, 173 (1928).
- [100] K. Iwaszczuk, M. Zalkovskij, A. C. Strikwerda, and P. U. Jepsen, Optica **2**, 116 (2015).

## 요약 (국문초록)

이 논문에서는 회절한계보다 훨씬 작은 구조인 나노갭에서 일어나는 빛의 구속 현상과 이를 이용한 포토레지스트 중합 현상에 대해서 다루었다. 나노갭의 폭은 수백 나노미터부터 10 나노미터 이하까지 다양하게 제작되었으며, 슬릿 구조, 슬랏 안테나, 보타이 안테나 구조 등 다양한 모양으로 제작되었다. 각각의 나노갭은 자외선의 투과 특성이나 테라헤르츠파의 공진 특성에 맞춰 제작되었다. 자외선 영역의 실험에서는 10 나노미터 이하의 폭을 가지는 크롬 나노갭과 일반적인 마스크 정렬 노광장치의 자외선을 이용하여 수행하였고, 회절 한계 이하 영역에서 나노리소그래피를 구현했다. 테라헤르츠 영역에서는 강한 테라헤르츠 펄스와 나노갭을 이용해서 회절 한계 이하에서 포토레지스트 중합을 구현했고, 이러한 포토레지스트 중합의 원인이 다중 광자 흡수보다는 전자의 전계 방출 때문임을 보였다. 해당 연구들은 유한요소해석법과 같은 시뮬레이션이나 파울러-노드 하임 방정식과 같은 이론 계산을 통하여 검증되었고, 나노갭이 회절 한계 이하 영역에서의 포토레지스트 중합, 또는 화학반응에 사용될 수 있음을 보였다. 이러한 연구들은 다양한 나노-광화학 연구에 새로운 통찰력을 제시할 것이다.

키워드: 나노갭, 포토레지스트 중합, 파장보다 작은 구조

학번: 2013-20367

# List of Publications

1. T. H. Kim, J. -G. Yoon, S. H. Baek, **W. Park**, S. M. Yang, S. Y. Jang, T. Min, J. -S. Chung, C. -B. Eom, T. W. Noh, '*Energy landscape scheme for an intuitive understanding of complex domain dynamics in ferroelectric thin films*', **Scientific Reports**, 5, 11625 (2015).
2. **W. Park**, J. Rhie, N.Y. Kim, S. Hong, D. -S. Kim, '*Sub-10 nm feature chromium photomasks for contact lithography patterning of square metal ring arrays*', **Scientific Reports**, 6, 23823 (2016).
3. **W. Park**, Y. Lee, T. Kang, J. Jeong, D. -S. Kim, '*Terahertz-driven polymerization of resists in nanoantennas*', **Scientific Reports**, 8 (1), 7762 (2018).
4. H. Kim, S. B. Choi, S. S. Choi, **W. Park**, C. C. Byeon, '*Extraordinary Transmission of Light Through Freestanding Au Films with Subwavelength Apertures and Double Slits*', **Journal of the Korean Physical Society**, 74 (2), 164-167 (2019).
5. S. Bahn, S. B. Choi, **W. Park**, H. Y. Jeong, K. H. Park, '*Fabrication of Si-based AFM Probe with High Q-factor for Fast Non-Contact Mode Scanning*', **Journal of the Korean Physical Society**, 74 (2), 94-97 (2019).
6. G. Ji\*, **W. Park\***, H.-T. Lee, C. -Y. Song, C. Seo, M. Park, B. Kang, K. Kim, D. -S. Kim, H.-R. Park, '*Terahertz time domain spectroscopy of GdBCO superconducting thin films*', **Progress in Superconductivity and Cryogenics**, 21 (1), 15-17 (2019). (\*equal contribution)
7. H. Kim, **W. Park\***, K. Nam, H. S. Jang, B. H. Kim, S. B. Choi\*, '*Effects of Electron Beam Irradiation on the Friction and Work Function of the Wrinkled Graphene*', **Under Review**. (\*corresponding author)

# Conferences

1. **W. Park**, J. Rhie, N. Y. Kim, S. Hong, D. -S. Kim, ‘Sub-10 nm chromium nanogap arrays for photomask applications’ , **Korean Physical Society**, Daejeon, Korea, 20-22 April 2016. (**\*Best poster presentation award**)
2. **W. Park**, Y. Lee, T. Kang, J. Jeong, D. -S. Kim, ‘Terahertz-photoemission-induced polymer crosslinking in nanoantennas’ , **Korean Physical Society**, Changwon, Korea, 24-26 October 2018. (**\*Best presentation award**)
3. **W. Park**, Y. Lee, T. Kang, J. Jeong, D. -S. Kim, ‘Terahertz-Induced Resist Polymerization in Nanoantennas’ , **Nature Conference on Nanophotonics and Integrated Photonics**, Nanjing, China, 9-11 November 2018.